International Journal of Earth Sciences (2023) 112:197–216
https://doi.org/10.1007/s00531-022-02254-6

ORIGINAL PAPER

# Geophysical and geochemical multi-method investigations for reconstructing subsurfaces, alluvial sedimentology, and structural geology (Tiber valley, Rome)

**Francesca Giustini[1] · Mauro Brilli[1] · Giorgia Carlucci[1] · Giancarlo Ciotoli[1,2] · Iolanda Gaudiosi[1] · Marco Mancini[1] · Maurizio Simionato[1]**

Received: 11 October 2021 / Accepted: 5 October 2022 / Published online: 27 October 2022

**Abstract**

Geophysical and geochemical methods were applied to detect the subsurface setting of an Upper Pleistocene-Holocene fluvial incised-valley where a travertine body intercalates between alluvial deposits of the Tiber river (central Italy), at Prima Porta (close to Rome). This study allowed us to provide more information regarding the local stratigraphic architecture and structural features, as a reference analogue to similar settings: i.e., hard (stiff) lithic travertines buried below fine and loose alluvial plain covers. Two Electrical Resistivity Tomography (ERT) profiles, interpreted and calibrated using previously collected litho-stratigraphic data from a borehole, identified a massive body, with a relatively high resistivity that correlates with the travertine deposit of Prima Porta. In addition to ERT, ambient noise measurements, processed with the HVSR technique and 2D array, and seismic refraction tomography were carried out; HVSR data were highly consistent with ERT results and allowed to discriminate between the travertine body and the silty-sand channels and overbank deposits, which were attributed to the Tiber river's evolution during Upper Pleistocene-Holocene. Finally, the presence of cracks/fractures could be inferred, as suggested by slight polarisation effects recorded in the HVSR results and soil-gas anomalies.

**Keywords** Buried travertine deposit · Electrical resistivity tomography · Ambient noise measurement · Soil-gas survey · Tiber valley · Upper pleistocene · Holocene

## Introduction

Geophysical methods, such as seismic methods, ground penetrating radar, and electrical resistivity tomography, are widely used to detect the subsoil structures of recent alluvial plains, where the lack of adequate outcrops prevents a detailed reconstruction of buried stratigraphic and morpho-structural elements (Bridge 2003; Miall 2014). Similarly, in these settings (i.e., alluvial plains), geochemical investigations have been used to infer the presence of morpho-structural discontinuities buried below the sediment cover (Klusman 1993; Ciotoli et al. 2007).

Here, we propose an integrated geophysical-geochemical approach aimed at defining the main features of the shallow subsoil of a portion of alluvial plain in the Tiber valley, central Italy, just north of Rome; this portion is considered as a case study and possible methodological reference for similar settings.

The Tiber valley corresponds to an NNW–SSE trending extensional basin that has been developing since the early Pliocene along the western flank of the central Apennines (Funiciello and Parotto 1978; Malinverno and Ryan 1986; Barberi et al. 1994). Most of the basin-fill consists of fluvial and deltaic deposits; the most recent deposits, which pertain to the valley's actual alluvial depocenter, consist of gravels and sands or silty sands alternating with floodplain muds. As a morpho-tectonic depression of extensional origin, the valley is bounded by dominant NNW-SSE trending normal faults and subordinate transversal fault systems, which may represent important routes for ascending, mineralised hot

---

✉ Francesca Giustini
francesca.giustini@igag.cnr.it

[1] Istituto di Geologia Ambientale e Geoingegneria, CNR, Area Della Ricerca di Roma1, Via Salaria Km 29,300, Monterotondo Stazione, 00015 Rome, Italy

[2] Istituto Nazionale di Geofisica e Vulcanologia, Sezione Roma1, Via di Vigna Murata 605, 00143 Rome, Italy

waters whose manifestations are visible in some places, especially along the borders (such as those which emerge in our case study) but also towards the centre (Giustini et al. 2018); in general, the deposition of continental carbonate bodies associated with these manifestations is always evident. In fact, especially along its western boundary, several deposits of continental carbonates crop out and/or are locally buried under the prevailing siliciclastic alluvial deposits of the Tiber river (Tentori et al. 2016; Giustini et al. 2018). The reconstruction of the sedimentary sequence within the central portion of the valley is impossible unless drilled cores are investigated.

Recently, an Upper Pleistocene travertine body of about 4 m in thickness, intercalated between Holocene and upper Pleistocene alluvial deposits, was identified in an 18 m deep borehole at Prima Porta, north west of Rome, and at a distance of 400 m from the right bank of the Tiber river, (Giustini et al. 2020). The borehole, drilled for agricultural water supply, revealed $CO_2$-dominated free gas emissions and the presence of mineralised, hypothermal waters that were recorded a few metres below the field level.

To comprehend the alluvial sedimentary sequence and the travertine body in relation to the gas emissions, the groundwater, and the local structural geology, a knowledge of the subterranean sedimentary setting is needed. Geophysical methods may conveniently be used for this type of investigation. In the present paper, we investigated the subterranean sediment sequence of Prima Porta using Electrical Resistivity Tomography (ERT) which allows remarkable penetration depths even if the presence of fluids can mask the geoelectrical contrasts between geological formations (Loke and Barker 1996; Loke and Dahlin 2002). The ERT technique has been successfully applied in several studies in which travertines were embedded within different sediments (Qarqori et al. 2012; De Filippis et al., 2013; Pola et al. 2014; Huerta et al. 2016; Török et al. 2019). In the present paper, ERT was coupled with spectral measurements of seismic ambient noise (Horizontal to Vertical Spectral Ratio—HVSR technique) (Nakamura 1989; Lunedei and Malischewsky 2015; Sánchez-Sesma 2017, and references therein). This technique was used to study subsoil settings by means of determining the seismic velocity contrasts that locate interfaces between sedimentary bodies with different mechanical characteristics. As an area characterised by rising mineralised waters and natural gases, geochemical soil-gas prospection was also used to investigate the most likely routes of fluid flowing through the strata up to the atmosphere in subterranean settings (Klusman 1993; Ciotoli et al. 2007).

The aim of this study is to test a multimethod approach for reconstructing buried stratigraphic and structural features and demonstrate their complementarity and ability to compensate for the limits of each one.

## Geological framework

The study area is located in the lower valley of the Tiber river, north of Rome and west of the central Apennines (Fig. 1a). The investigated Prima Porta site is located in the Tiber alluvial plain which crosses, along the NNE-SSW direction, a hilly belt consisting of Pliocene–Quaternary sedimentary and pyroclastic deposits. In particular, the study area lies in the inner convex bank of an eastward-directed meander of the Tiber (Fig. 1b).

Structurally, the valley corresponds to a morpho-tectonic depression of extensional origin, the Rome Basin, bounded by dominant NNW-SSE trending normal faults and subordinate SW-NE directed transfer faults; short N-S trending dextral strike-slip faults are also found within the basin (Faccenna and Funiciello 1993).

Since the Early Pliocene, the extensional regime related to the opening of the Tyrrhenian Sea back-arc basin has controlled the growth and development of the Rome basin (Funiciello and Parotto 1978; Malinverno and Ryan 1986; Barberi et al. 1994). The pre-rift succession comprises Trias to Miocene calcareous, cherty, and siliciclastic pelagic sequences, which were stacked to form the Apennine Chain fold-thrust belt during the Tortonian-Messinian (Patacca et al. 1990; Cosentino et al. 2010). The Pliocene–Quaternary syn-rift successions consist of marine, transitional, and continental sediments (up to 1 km in thickness) covering the pre-rift limestones and turbidites with an angular unconformity.

Since the late Early Pleistocene (~ 1.3 Ma), active uplift has affected the whole area, which has led to the emergence of the former sea floor. This phase was dominated by the fluvial sedimentation of the juvenile Tiber river ("Paleotiber" in Funiciello et al. 1994; Mancini and Cavinato 2005; Mancini et al. 2007) and by the deposition of eruptive products from the Sabatini Mts and Albani Hill volcanic districts (De Rita et al. 1993; Sottili et al. 2004; Funiciello and Giordano 2010). The ancient Tiber river incised the Pliocene-Early Pleistocene marine clay and silt defining an NNW-SSE trending deep paleo-valley, filled with gravels, sands, and minor mud. These deposits rarely crop out since they are buried below younger pyroclastic successions (ignimbrites, phreato-magmatic ashes, pumice, and ash falls), dated at approximately 600–280 ka (Barberi et al. 1994), and locally by Upper Pleistocene-Holocene fluvial deposits.

The Prima Porta site is, in fact, located on the west side of the recent Tiber's alluvial plain that, in this area, is ~ 2 km wide and has elevations ranging from 19 to 22 m above sea level (Fig. 1b). NNW-SSE trending normal faults, inferred from Funiciello et al. (1992), bound the ancient paleo-valley to the north-east and are those and are

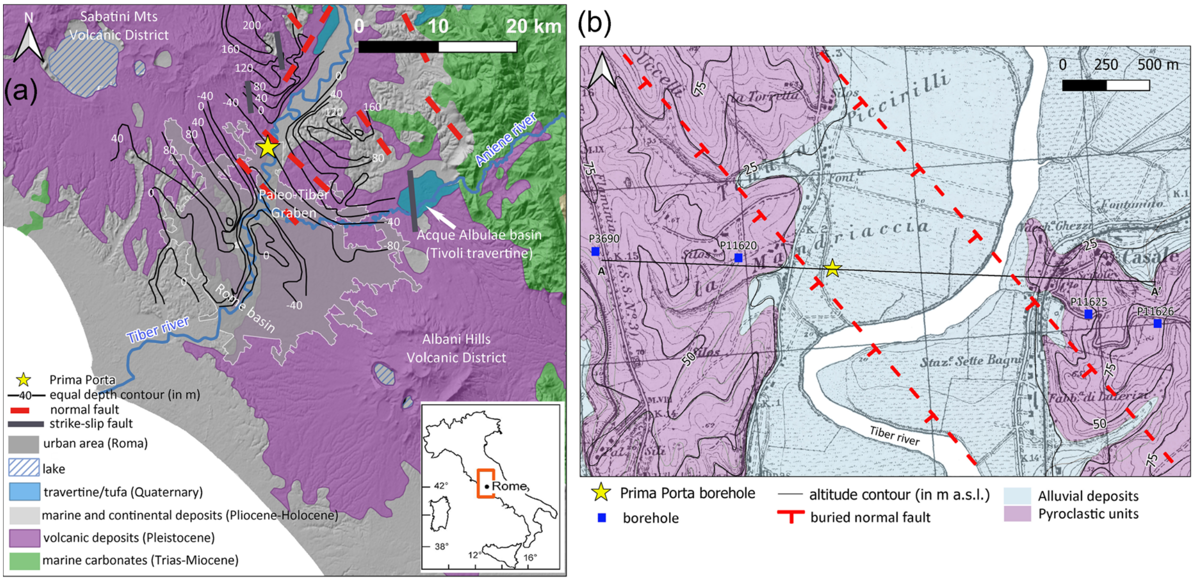

**Fig. 1** **a** Geological map of the Tiber valley showing the location of the Prima Porta site: geology from SGI-ISPRA, faults from Faccenna (1994), equal depth contour from Funiciello et al. (1992); **b** Sketch map of the Prima Porta area: geology from the Geological Map of the Lazio Region, scale 1:25,000 and topography from 1:25,000 topographic maps of Italy from the Istituto Geografico Militare. The trace of the cross section A-A′ (Fig. 2a), location of the boreholes (from Ventriglia 2002; Di Bella et al. 2002), and buried inferred normal faults (from Funiciello et al. 1992) are also drafted. Modified from Giustini et al. (2020)

related to the development of the Paleotiber graben, buried by younger pyroclastic successions and fluvial deposits.

The alluvial plain corresponds to the top of the fluvial incised-valley fill of the Upper Pleistocene-Holocene Tiber Depositional Sequence or TDS (Milli et al. 2016) (Fig. 2a). The last cycle of sea level changes (from MIS5d to MIS1; 116–0 ka) controlled the valley fill, which comprises the complex stack of deposits belonging to the lowstand to transgressive and highstand systems tracts, totalling a thickness of 60 m.

The oldest TDS deposits are attributed to the early lowstand phase (116–26 ka) and define rare depositional terraces perched on the incised-valley slopes and buried below more recent transgressive sediments. These terraces record short-lived phases of sedimentation which occurred during the long phase of the lowering of base level.

Younger basal gravels organised into amalgamated channel bodies in the deepest portion of the incised valley and overlaying channel sand and floodplain muds, are, respectively, ascribed to the late lowstand-early transgressive (26–14 ka) and late transgressive-highstand (14–0 ka) phases (Milli et al. 2016). In particular, the sands define channel-fill bodies with different stacking patterns for the transgressive and the highstand systems tracts of TDS (Milli et al. 2016), also related to the laterally confining floodplain fines: from relatively narrow and vertically accreted channel bodies of the transgressive systems tract, with high rates of accommodation, to wider and laterally amalgamated channel bodies of the highstand systems tract, with decreasing rates of accommodation and increasing channel clustering (see also Schumm 1993).

The stratigraphy of the 18 m-long core recovered at Prima Porta (Fig. 2b) corresponds to one of the detached depositional terraces and overlying transgressive sediments (Giustini et al. 2020): above the basal layer, which consists of 1.5 m thick yellow-beige massive silty sands, attributed to the Paleotiber unit (i.e., Fosso della Crescenza and Santa Cecilia Formations, in Funiciello and Giordano 2008), a 11 m thick body represents the buried terrace; this is part of the *Fiume Tevere* Synthem or TDS (according to Funiciello and Giordano 2008, or Milli et al. 2016, respectively), and consists of a 5.5 m thick succession of grey, massive pebby-silty sand and clay with sparse carbonate encrustations (unit a), ~ 4 m of travertine at Prima Porta (unit b), and ~ 1 m of massive dark brown/red clayey paleosols (Fig. 2b). The travertine was dated between 53.5 ± 10 ka to 24.2 ± 4.7 ka by U/Th method (Giustini et al. 2020) and can be correlated to the MIS 3. The remaining upper sequence consists of beige massive silt and clay that record the recent phases (age ≤ 6.0 ka, middle-late Holocene) of river flooding (unit c).

## The travertine of Prima Porta

The travertine of Prima Porta macroscopically consists of a hard and quite dense crystalline material, which appears to be structureless or with horizontally bedded and inclined

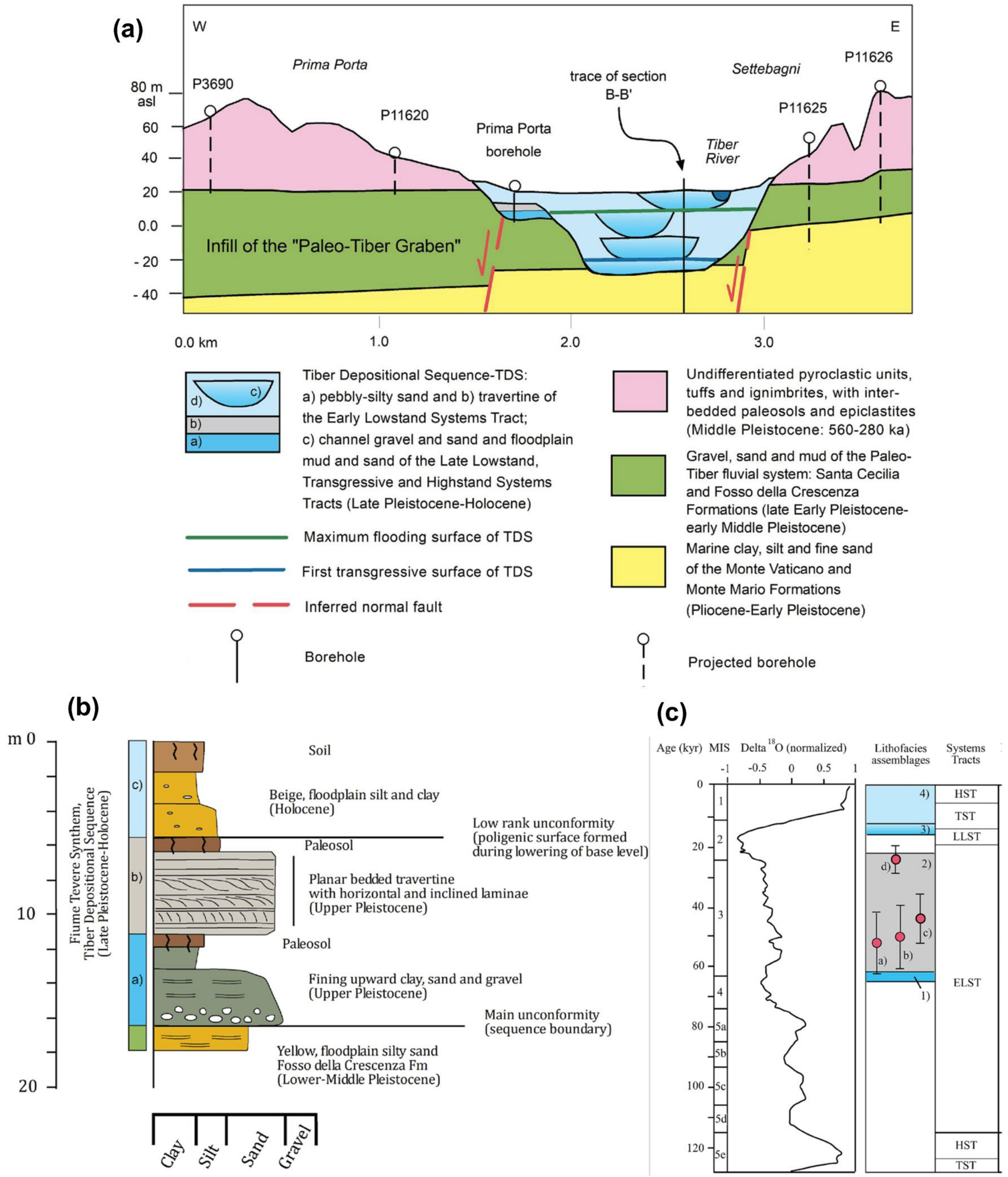

**Fig. 2** **a** Geological cross sections showing the stratigraphic architecture of the middle Tiber valley, based on the geological map of Funiciello and Giordano (2008) and borehole data from Di Bella et al. (2002) and Ventriglia (2002); **b** Schematic section of the drilled core; the travertine deposit is embedded within alluvial sediments of the Tiber river. Reproduced from Giustini et al. (2020); **c** Chronostratigraphic scheme of the Prima Porta deposit; Prima Porta travertine ages (red circles) are from Giustini et al. (2020), lithofacies assemblages correspond to the schematic section in **b**, oxygen isotope curve is from Martinson et al. (1987), Systems Tracts of the Tiber depositional sequence are based on Milli et al. (2016) (HST: Highstand Systems Tract; TST: Transgressive Systems Tract; LLST: Late Lowstand Systems Tract; ELST: Early Lowstand Systems Tract)

layers that are a few centimetres to decimetres thick. These features, as well as their microfacies associations (i.e., micrite crusts and rafts, both intercalated within and between the shrubs), suggest that the deposition of this travertine was associated with low-to-moderate energy environments, such as gently dipping, shallow pools of low-angle terraced slopes (Giustini et al. 2020). Currently, the travertine of Prima Porta is associated with hypothermal, saline water and

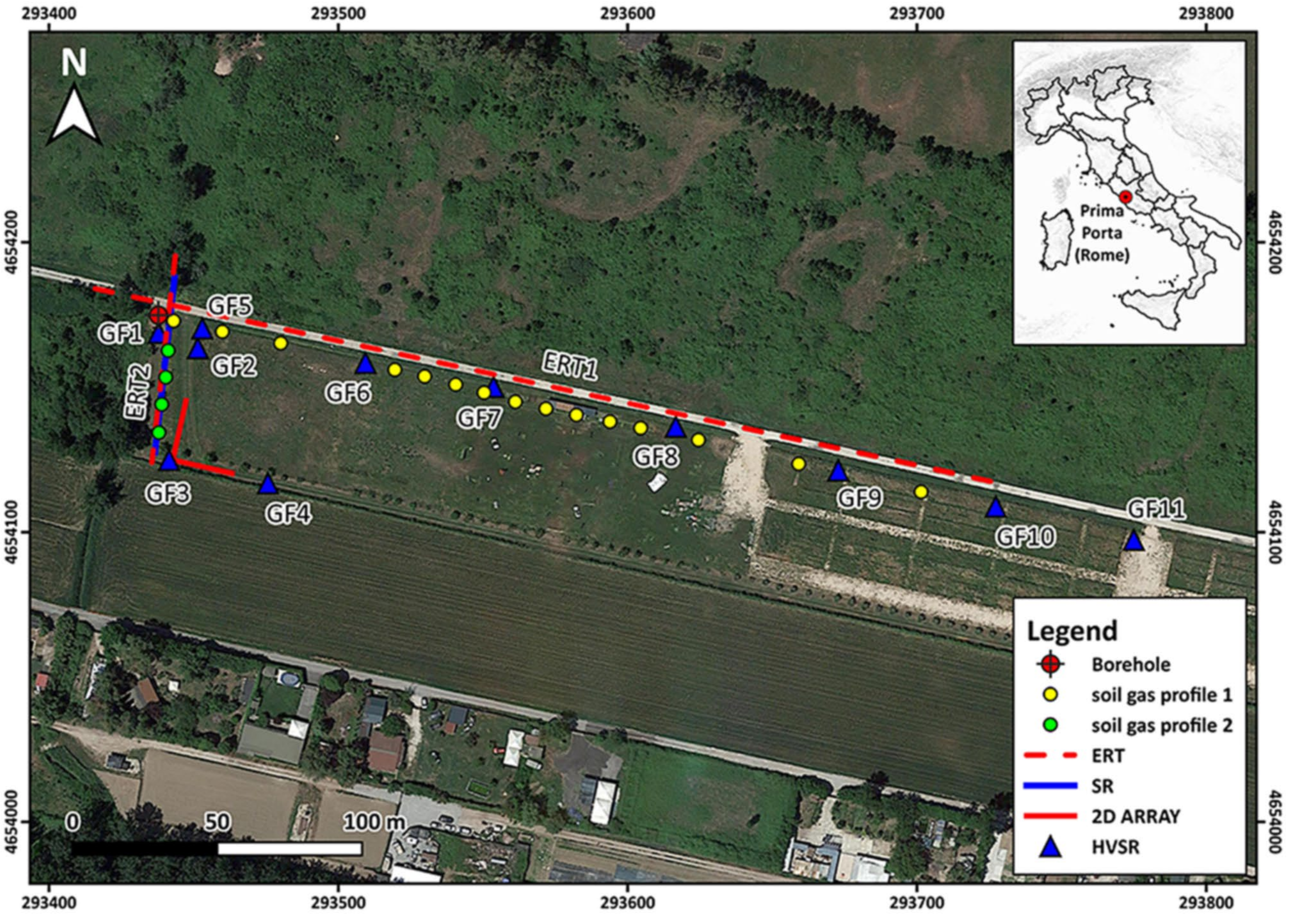

**Fig. 3** Aerial view of the study area with the location of the Prima Porta borehole, HVSR, 2D array, Electrical Resistivity Tomography (ERT), Seismic Refraction (SR) surveys, and soil-gas measurements

deeply derived $CO_2$ gas emissions, whose ascent through the rock units is probably connected with a crustal structural lineament (Giustini et al. 2018). Diagenetic alteration appears to be limited, as inferred from macroscopic and petrographic observations (Giustini et al. 2020). The travertine was dated between 53.5 ± 10 ka to 24.2 ± 4.7 ka by U/Th method (Giustini et al. 2020), its deposition started approximately coevally with the wettest climatic conditions occurring during MIS3 (Fig. 2c), whereas the end of the deposition period coincides with the cold and arid phase of the last glacial maximum (Giustini et al. 2020).

## Methods

Different methods were applied to study the subsurface setting of the study area, including: electrical (ERT), surface waves based (HVSR and 2D arrays), shallow seismic refraction, and geochemical ($CO_2$ and $^{222}$Rn soil-gas survey) methods. Each method was processed separately and then a joint interpretation was performed. The location of the measurements is shown in Fig. 3.

### Electrical Resistivity Tomography (ERT) Surveys

ERT surveys were carried out to determine the specific electrical resistivity ρ of the ground and to obtain 2D images of its distribution in vertical ground sections.

ERT consists of the application of a direct electrical current into the ground using a quadrupolar dispositive, the acquisition of A/D converted data of voltages through a computer-controlled acquisition system and the computation of resistivity using Ohm laws. The quadrupole consists of two current electrodes, through which direct current is fed into the ground, and two measuring electrodes, through which the voltage is measured. There are many different electrode array configurations available, but all configurations are aimed at gathering data that can be used to estimate lateral and vertical variations in ground resistivity values with different resolutions (Loke and Barker 1996; Loke and Dahlin 2002).

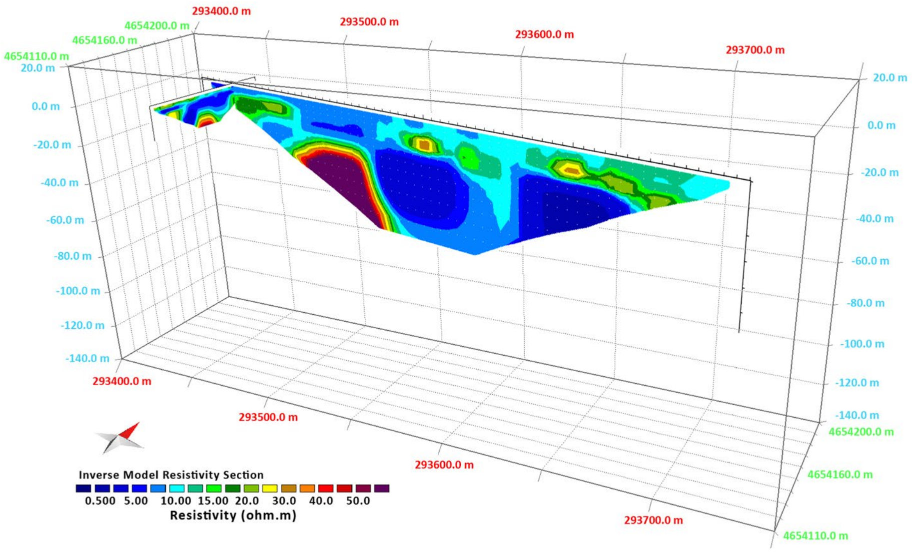

**Fig. 4** Inverted 2D resistivity models for the two perpendicular electrical resistivity tomographs. ERT-1 is oriented W–E; ERT-2 is oriented N–S. The models are displayed in perspective to visualise the 3D subsoil structure starting from the 2D cross-sectional images

Two ERT measurements were performed using a georesistivimeter 16SG model (Pasi, S.r.l.), equipped with 64 electrodes with variable spacing using the Wenner-Schlumberger configuration. As conventionally reported in the literature, the depth of investigation is up to 1/5 or 1/6 of the total length of the electrical profile. Data were processed using the Res2dinv software from Geotomo Software. The 2D inversion is based on the robust constrained least-squares inversion implemented with a Gauss–Newton method.

The first measurement (ERT-1) was carried out in the W-E direction, using 64-electrodes with a 5 m electrode distance, which allows the 2D reconstruction of the resistivity trend in the subsoil up to a depth of about 50 m along a 315 m long profile. The ERT-1 profile crosses the Prima Porta borehole—whose stratigraphy is known (Fig. 2b) and which was used to calibrate the resistivity measurement—down to electrode n. 40. The second measurement (ERT-2) was performed with an N–S orientation; in this case, 48 electrodes were used with an electrode distance of 1.5 m and a total length of 70.5 m, reaching a depth of about 12 m. The two arrays intersect between the electrodes n. 40 of the W–E array and n. 7 of the N-S one, as shown in Fig. 4.

## Ambient Noise Survey

A series of eleven ambient noise measurements, labelled from GF1 to GF11, was conducted along the two cross-sections (Fig. 3). The equipment consisted of SS02 SARA velocimetric sensors with a cut-off frequency of 0.2 Hz, connected to six-channel SL06 SARA data loggers. Data were recorded with a sample rate of 200 samples per second. During installation, particular care was adopted to deploy sensors to guarantee an adequate coupling with the ground and to avoid the positioning of the sensors directly over sources of disturbance. Shallow holes were realized to emplace sensors and remove the possible disturbance of the grass.

Recordings of about one hour of noise were collected and the Horizontal to Vertical Spectral Ratio (HVSR) technique was applied (Nakamura 1989). This is a well-established approach: inferences for the subsurface seismic velocity contrasts may be extrapolated from the retrieved peaks in the HVSR curves, considering for instance that shallower interfaces produce higher peak frequencies. Each ambient vibration recording was divided into 50 s-long time windows in the open-source software Geopsy (http://www.geopsy.org/) (Wathelet et al. 2020). We computed the amplitude spectra for the vertical and horizontal components (north and east components). Spectra were smoothed using the Konno and Ohmachi (1998) window with a *b* value of 40, while the horizontal spectra were computed from the north and east components as: $\sqrt{(\mathrm{north}2+\mathrm{east}2)}$ before computing the HVSR for each time window. Then, we computed the average HVSR for each station.

In addition to the HVSR noise measurements at single stations, surface-wave methods were also applied, allowing the acquisition of 2D array ambient vibrations data and one S-waves velocity profile. The latter was retrieved from a joint inversion of Rayleigh dispersion curves with ellipticity. In more detail, 2D arrays are based on the acquisition of ambient vibrations and the interpretation of the recordings obtained at synchronised seismic stations, or geophones (seismic antenna) with the ground, according to different geometries. The geophones were arranged in a two-dimensional L-shaped geometry with regular spacing (3 m on each side; see also Fig. S4b in Supplementary Materials). Even if more regular and symmetrical shapes (circular or triangular shapes) are recommended in general, T or L shapes are also possible (Foti et al. 2018). Thus, an

L-shaped geometry can be a compromise among the number of sensors, the operating time available and a desired highest resolution of the uppermost layer description. In this case, the choice of limited inter-geophonic distance (3 m) and the consequentially maximum dimension of each branch lower than 36 m agreed with the necessity of exploring the presence of lateral heterogeneities and the first uppermost layers. The basic scheme of the application of all surface-wave methods consists of three steps: (i) measuring the wave trains of surface waves by means of the arrays of seismic stations or geophones, suitably deployed on the surface; (ii) estimating the apparent dispersion curve of surface waves; and (iii) solving the inverse problem to estimate the soil structure looking for the best-fit between the experimental and theoretical dispersion curves. Joint inversions with the HVSR technique related to Rayleigh wave ellipticity are generally performed to obtain more robust representative S-waves velocity profiles. In this case, the dispersion curve was derived by applying two different methods: MSPAC (Modified SPatial Auto-Correlation, Bettig et al. 2005) and the conventional beamforming f–k (Lacoss et al. 1969). The registrations of the noise wave-field were performed for a minimum duration of 40 min with 24 vertical geophones (cut-off frequency equal to 4.5 Hz). Geophones are equipped with spikes that serves as a screw to secure the coupling with the ground. Also in this case, before emplacing geophones, the grass around each 1-component sensor was removed to avoid any possible disturbance. Different codes were used: the Geopsy software (www.geopsy.org) (Wathelet et al. 2020) was used to retrieve the dispersion curves for applying f-k and MSPAC analyses, while HV-inv (García-Jerez et al. 2013, 2016; Piña-Flores et al. 2017; Sánchez-Sesma et al. 2011) was used for solving the inverse problem. Hv-inv is based on the diffuse field assumption, therefore the resulting modelled ellipticity curve is comprehensive of both Rayleigh and Love waves. Rayleigh wave ellipticity used for the joint inversion was defined directly from the HVSR curve.

## Seismic Refraction Tomography Survey

Seismic refraction (SR) is generally applied to determine impedance contrast for engineering applications, to investigate the depth to bedrock, as well as for groundwater exploration, crustal structure, and tectonics (Kilner et al. 2005; Asokhai et al.2008; Varughese et al., 2011; Chiemeke and Aboh 2012). The seismic refraction method is based on the measurement of the travel time of seismic waves refracted at the interfaces between subsurface layers of different velocity (Ayolabi et al. 2009). The seismic signal is introduced into the subsurface via a shot point using an elastic wave generator. The energy generated either travels directly through the upper layer (direct arrivals) or down through the various layers before returning to the surface (refracted arrivals). It is then detected at the surface by a series of geophones (10 Hz), spaced at regular intervals. Both compressional waves (P-waves), which provide depth information about the interfaces, and shear waves (S-waves), which provide additional data about the engineering properties of the subsurface media, can be used in the seismic refraction method (Igboekwe and Ohaegbuchu 2011; Gabr et al. 2012). SR surveys use the process of critical refraction to infer interface depths and layer velocities. Based on the analysis and inversion of the field data, seismic profiles are constructed to evaluate the thickness and type of materials of the subsurface (Okiongbo et al. 2011). In this case study, the technique was usefully joined with the 2D array results: the P-waves profile obtained was applied as a constraint for the dispersion curve inversion. In particular, the Vp model obtained from the seismic refraction tomography survey was used as Vp profile max and min in the dispersion curve joint inversion. The resulting Poisson's ratio is about 0.5 and is comparable with the value assumed of the uppermost saturated deposits. The data are presented as cross-sectional plots representing the path, velocities, and depths of P-waves to various interfaces. SR was performed along the aforementioned ERT-2, using a geophone inter-distance of 2.5 m for a total length of 57.5 m.

## Soil–Gas Survey

Soil-gas measurements were performed along two profiles parallel to the ERT profiles, according to a sampling distance ranging from 20 to 40 m. Nineteen soil-gas samples were collected using a well-consolidated technique (Beaubien et al. 2013; Ciotoli et al. 2007) consisting of pounding a 6.4 mm, thick-walled, stainless-steel probe into the soil at a depth of about 0.6–0.8 m using a co-axial hammer; such a depth ensures the negligible influence of atmospheric air (Hinkle 1994). A portable multi-gas analyser (Draeger X-am 7000) directly connected to the probe was used to measure carbon dioxide ($CO_2$) concentrations directly in the field. Soil-gas radon ($^{222}Rn$) concentrations were measured with a portable RAD7 alpha detector (Durridge Company Inc.), performing three/four measurements of radon and thoron activity each, with a 5-min integration time, and using a drying tube (filled with $CaSO_4$) to maintain the relative humidity below 10%.

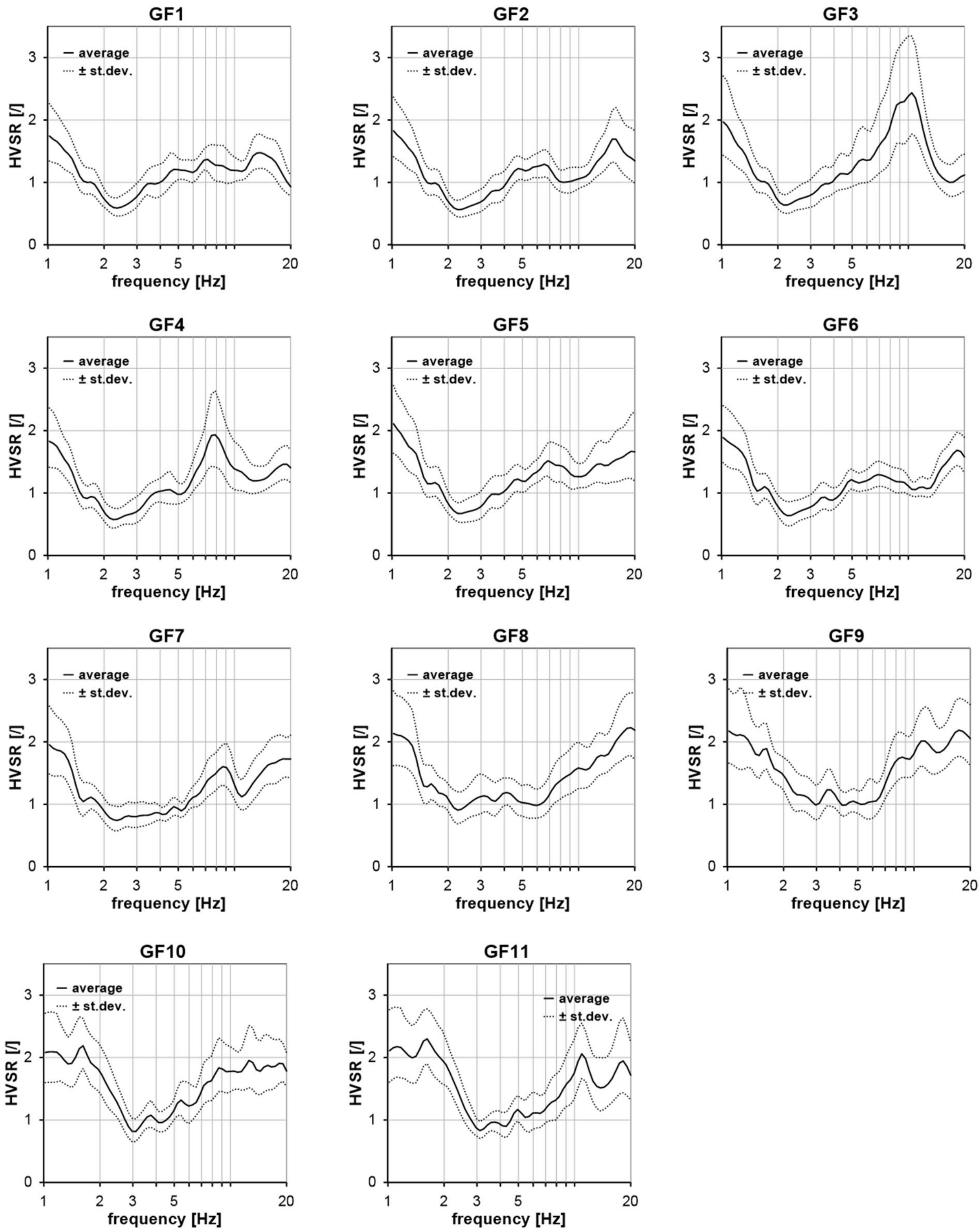

**Fig. 5** Measured HVSR curves. Single plots refer to the band 1–20 Hz for clarity. Curves plotted in the range 0.2–20 Hz may be found in the Supplementary Materials

## Results

### ERT Profiles

Two ERT profiles were performed along perpendicular directions. The first tomograph (ERT-1) was made in the W-E direction, across the valley, and the second (ERT-2) in N-S direction, down the valley and located in the innermost portion of the meander (Fig. 3). Resistivity values varied from 0.5 to 60 Ω × m; three zones could be distinguished on the basis of these values (Fig. 4).

Zone 1, characterised by low resistivity (< 15 Ω × m) is coloured in blue in Fig. 4. In ERT-1, this zone appears quite surficial between the metric coordinates of 80 and 150 m, and deeper than 20 m in the central-eastern part of the profile. In ERT-2, the zone of low resistivity is located below 1.5 m and appears as a sub-horizontal layer (about 3 m thick) that becomes increasingly deep between 40–50 m toward the south.

Zone 2 represents resistivities between 15 and 30 Ω × m, and is shown in green to yellow colours. In ERT-1, two levels with resistivities between 15 and 30 Ω × m are recognised in the eastern and western parts of the tomograph, disconnected by a low resistivity area in the centre. In ERT-2, Zone 2 is located just below the surface and is about 1.5 m thick. In addition, a level with resistivities between 15 and 30 Ω × m displays a concave-upward section wedging out toward the central part of the profile, where the resistivity tends to increase up to 50 Ω × m. Finally, a lens of Zone 2 is located in the eastern part of the profile, embedded within a low resistivity area.

Zone 3 is characterised by the highest resistivities (> 30 Ω × m), shown in orange to purple colours. Zone 3 is well represented in ERT-1 by a resistant block with a sharp lateral variation of resistivity in the central-western part of the profile, whose top is at a depth of about 20 m.

### Ambient Noise Survey

Results from noise measurements in terms of HVSR and single spectra are reported in Figs. 5 and 6, respectively.

HVSR amplitude never overcomes the value of 2.5; therefore, a smooth change in impedance properties is expected.

Moreover, as seen in Fig. 5, the mean HVSR at the GF1 to GF7 sites has amplitude values lower than 1, between about 2 and 4 Hz; this may be associated with an inversion of S-wave velocity in the soil profile, i.e., the upper sediments have a higher S-wave velocity than the underlying layers. Single spectra in Fig. 6 would show a behaviour traceable to stratigraphies with similar characteristics. In this case, the amplitude of the vertical component at the same range of frequencies increases from the GF1 to GF5 and GF1 to GF7 sites and the vertical component has higher values than those of the horizontal components. In these cases, as suggested by Castellaro and Mulargia (2009), local minima of the vertical component associated with flat or local maxima in the horizontal ones have to be carefully considered, since they may hide important HVSR peaks such as the one at 2.5 Hz.

Otherwise, both HVSR and single spectra at the GF8, GF9, GF10, and GF11 sites show the expected behaviour in the case of a soil profile with S-wave velocities increasing with depth.

From the analyses of the single spectra, despite the high variability of the measured HVSR curves, it arises that the predominant frequency f of the study area is 1.5 Hz in the range 1–10 Hz. A further peak occurs at frequencies lower than 0.8 Hz. This is relative to the Tiber river valley resonance referring to the deepest bedrock interface (see Carlucci 2017; Marcucci et al. 2019 and reference therein), and it was not considered because our study only focuses on the characterisation of the first layers (up to 30–40 m in depth). Another peculiar shape is recognisable at frequencies greater than 5.

All these considerations led us to group the HVSR into three different clusters. The first cluster exhibits a bi-modal shape (in blue in Fig. 7); the second cluster shows a very broad band peak at a higher frequency which may be related to a 2D/3D subsoil model; and the third cluster shows a peak with very high amplitude values and one with HVSR characterised by the clearest peaks (grouping GF3 and GF11). Both of them are quite different from those retrieved at stations in their immediate vicinity, but further data would be necessary to retrieve insights about this behaviour.

Wavefield polarisation analysis was also applied to the ambient noise measurements (Fig. 8). The GF1, GF3, and GF4 stations show a slight polarisation with an azimuth of N80-100° for frequencies > 6 Hz; the GF7 and GF8 records have a similar characteristic, but with a slightly lower azimuth (N0-20°). The GF5 and GF6 stations seem to show transitional behaviour. The peaks in the range 0.2–1 Hz show a N120° polarisation in almost all the measurements (see Supplementary Fig. 1). This analysis may reveal the possible presence of high angle to subvertical structural or paleo-morphological discontinuities within the sedimentary complex as they may tend to align the waves' oscillation plane perpendicular to or at a high angle to the direction of the lineaments themselves.

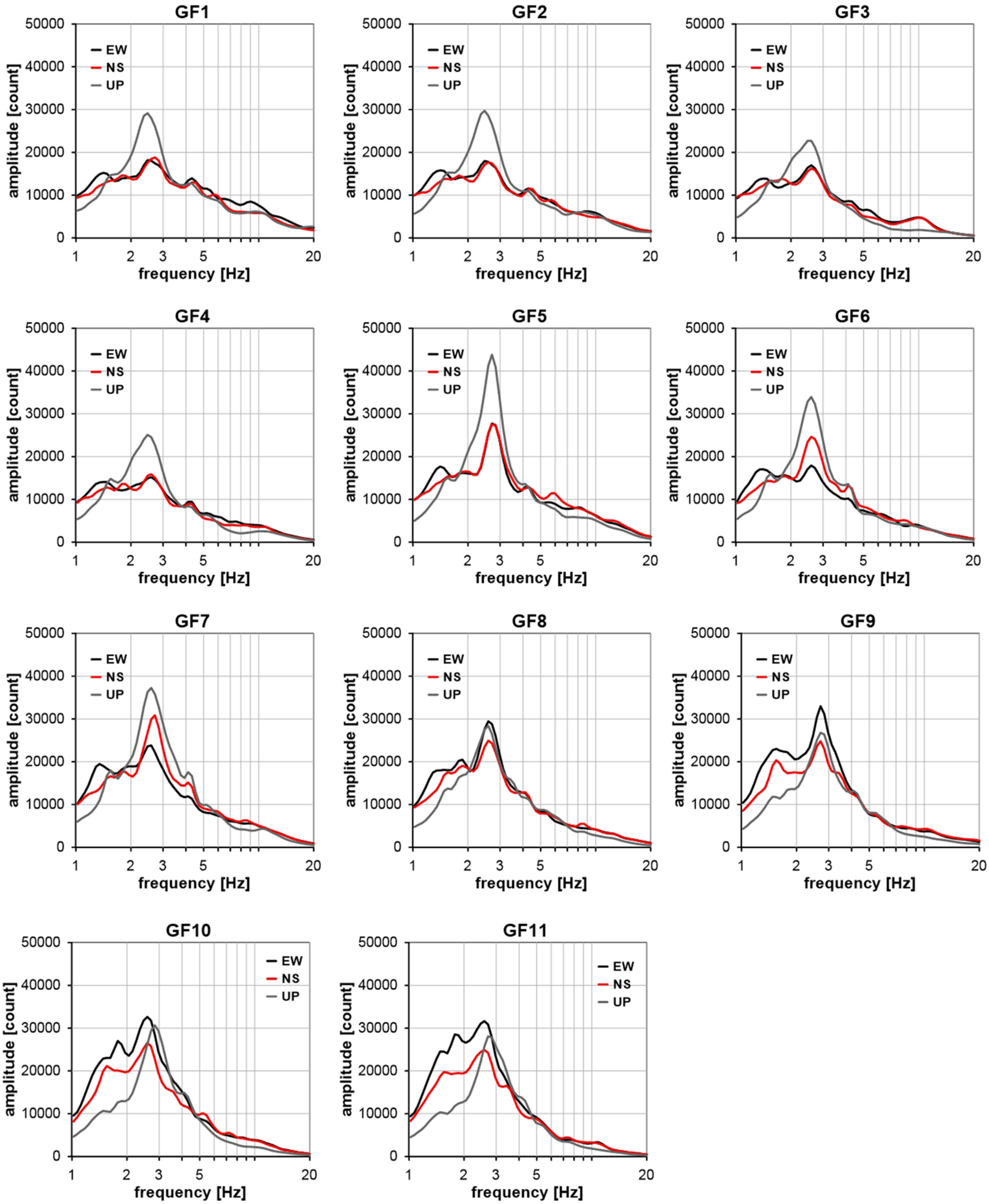

**Fig. 6** Measured single spectra curves. Single plots refer to the band 1–20 Hz for clarity. Curves plotted in the range 0.2–20 Hz may be found in the Supplementary Materials

Regarding the 2D array measurement, since one of the hypotheses at the base of this method is the assumption of an infinite semi-space with parallel layers, before computing the dispersion curve, a control was made on the single spectra of the vertical component acquired at each geophone. This analysis led to the exclusion of eight geophones (four at each extreme of the L-shaped array). The

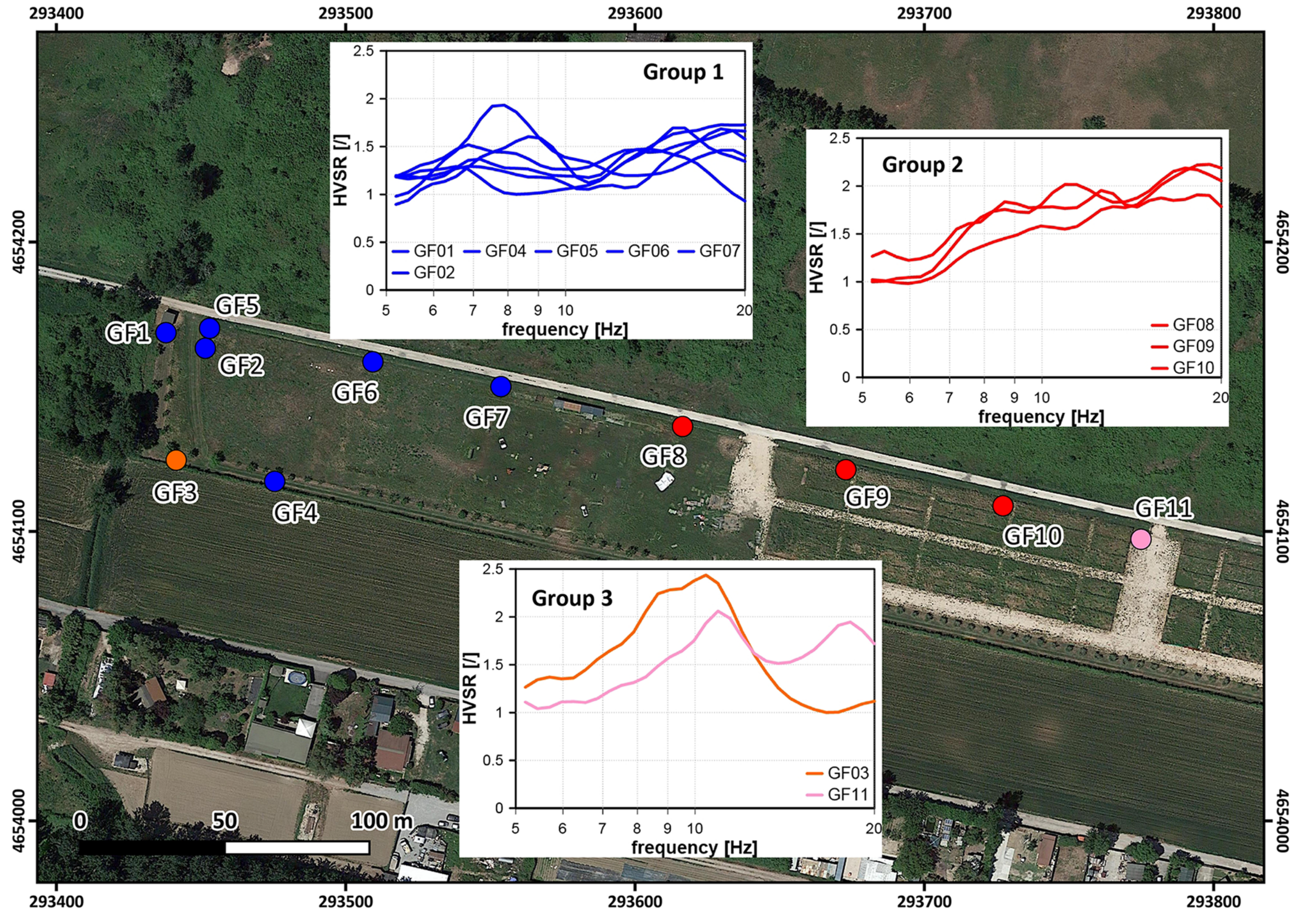

**Fig. 7** Groups of HVSR curves

variability of the vertical components on all the geophones of the array is shown in Supplementary Fig. 2.

The results from the 2D array are shown in Fig. 9. These latter, as well as the frequencies highlighted by the HVSR curves, are useful for making inferences about the site's characterisation. Regarding the agreement shown in Fig. 9b, we have overlapped the peaked f–k and MSPAC dispersion curves. Results showed that the combination of different methods (f–k and MSPAC techniques) give complementary results. Average dispersion curves are comparable in the range 9–13 Hz for both techniques, and this increases the confidence about the results while peaking the f-k dispersion curve out of the bounds of the results obtained from MSPAC, remaining into the kmax and kmin limits, allows extending the imaging towards highest frequencies. The general trend of the MSPAC curve seems similar to the best-fit, while this latter is within the average and ± standard deviation f–k dispersion curves.

## Soil–Gas Profiles

Soil-gas concentrations ($CO_2$ and $^{222}Rn$) were measured along two profiles parallel to the ERT acquisitions, to verify the presence of possible structural or buried morphological discontinuities (faults, fractures, buried scarps) which provide routes for deep-gas leakages in correspondence to the low resistivity areas recognised in the ERT profiles. The data are reported in Table 1; the soil-gas samples exhibited concentrations of up to 10.6% for $CO_2$ and up to 7.98 kBq/m$^3$ for $^{222}Rn$.

Along profile 1 (Fig. 10a), the spatial distribution of $CO_2$ and $^{222}Rn$ values shows two peaks that occur between 100 and 150 m, in correspondence with the low resistivity zone observed along ERT-1.

Along profile 2 (Fig. 11a), the highest $^{222}Rn$ activity (7.98 kBq/m$^3$) was measured at the southern end of the profile, in correspondence with the high resistivity zone observed in the ERT-2 profile; $CO_2$ concentrations follow a trend similar to radon isotopes, but their values are relatively lower (up to 3.6%) than those measured along profile 1.

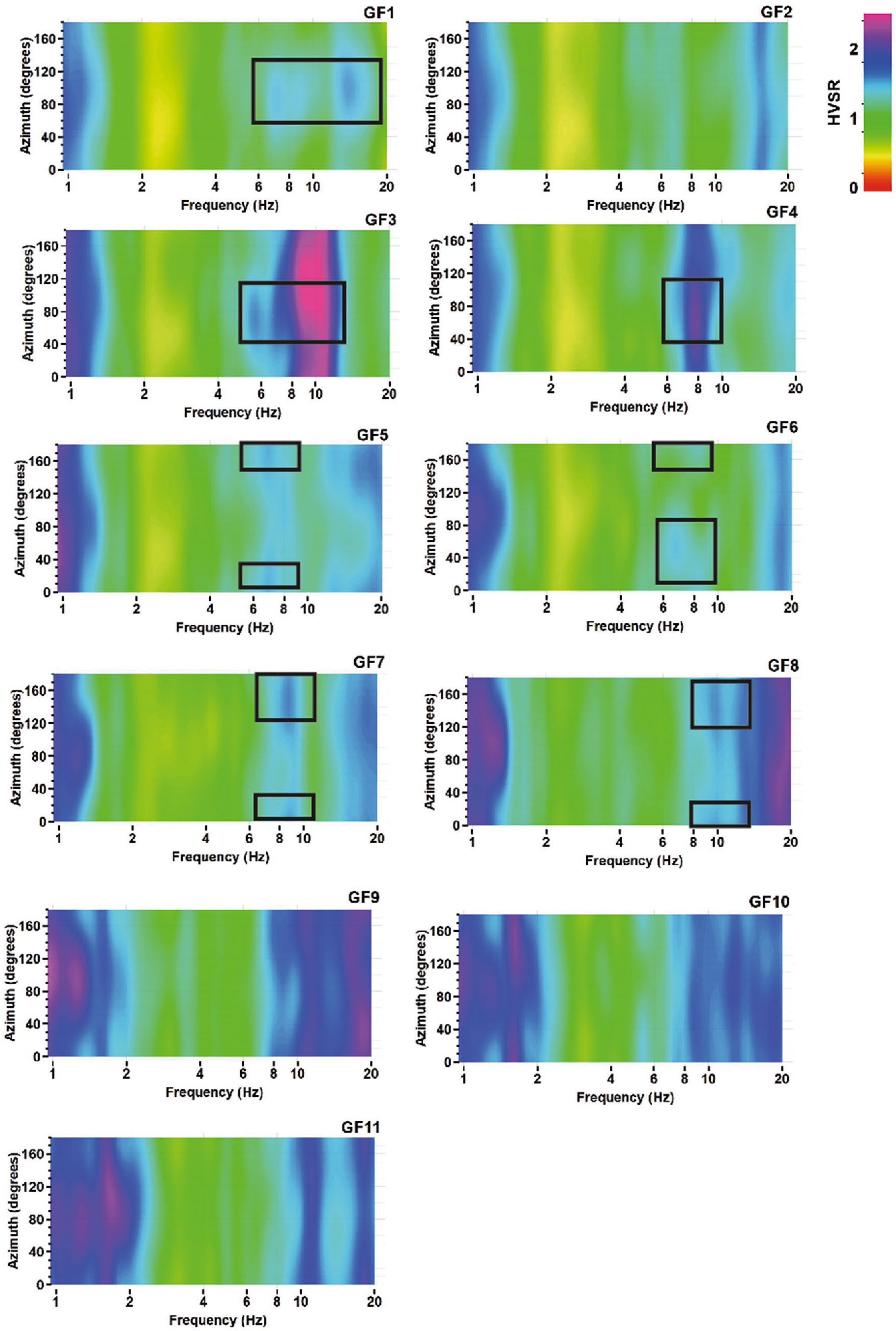
GF1
GF2
GF3
GF4
GF5
GF6
GF7
GF8
GF9
GF10
GF11
Azimuth (degrees)
0
40
80
120
160
Frequency (Hz)
1
2
4
6
8
10
20
HVSR
0
1
2

◂**Fig. 8** Rotational HVSR results for each station, referring to the band 1–20 Hz for clarity: HVSR curves plotted in the range 0.2–20 Hz may be found in the Supplementary Materials. Black boxes indicate the main polarisations: measurement at GF1 and GF3 sites show a slightly polarisation with an azimuth of N80-100° for frequencies > 6 Hz, measurements at GF5 and GF6 sites show amplification in the band N0-20° and about N160-180°; measurement at GF7 and GF8 sites show amplification in the band N0-20° and in a wider azimuthal range (about N120-180°)

## Interpretation of data and discussion

The correlation between borehole stratigraphy, geomorphological observations, geophysical, and geochemical data provides clues about the surface and subsurface geometry of the Prima Porta travertine body and the embedding sediments which are useful for better defining the stratigraphic and morpho-structural architecture of this sector of the Tiber valley.

In plan-view, the Prima Porta meander is featured by the lateral stack of several, east-directed, and convex-shaped scroll bars (Fig. 12), which suggests a generalised eastward expansion of the entire meander point-bar and river-channel system. Indeed, scroll bars typically record the incremental growth of a point-bar (Russell et al. 2018, with references); in this case, they have been identified on the map and on Google Earth images by small topographic irregularities (i.e., ridges and swales), by alignments of localised creeks, and by alternating belts of different soil moisture and vegetation cover densities.

Regarding the subsoil structure, since the ERT-1 survey was performed in correspondence with the Prima Porta borehole, it was possible to calibrate the ERT results and to directly correlate resistivity values with the litho-stratigraphic characteristics. From top to bottom, the borehole, whose stratigraphy is shown in Fig. 2b, intercepts alluvial sediments (silt and clay of floodplain environment) attributed to the most recent phase of deposition of overbank

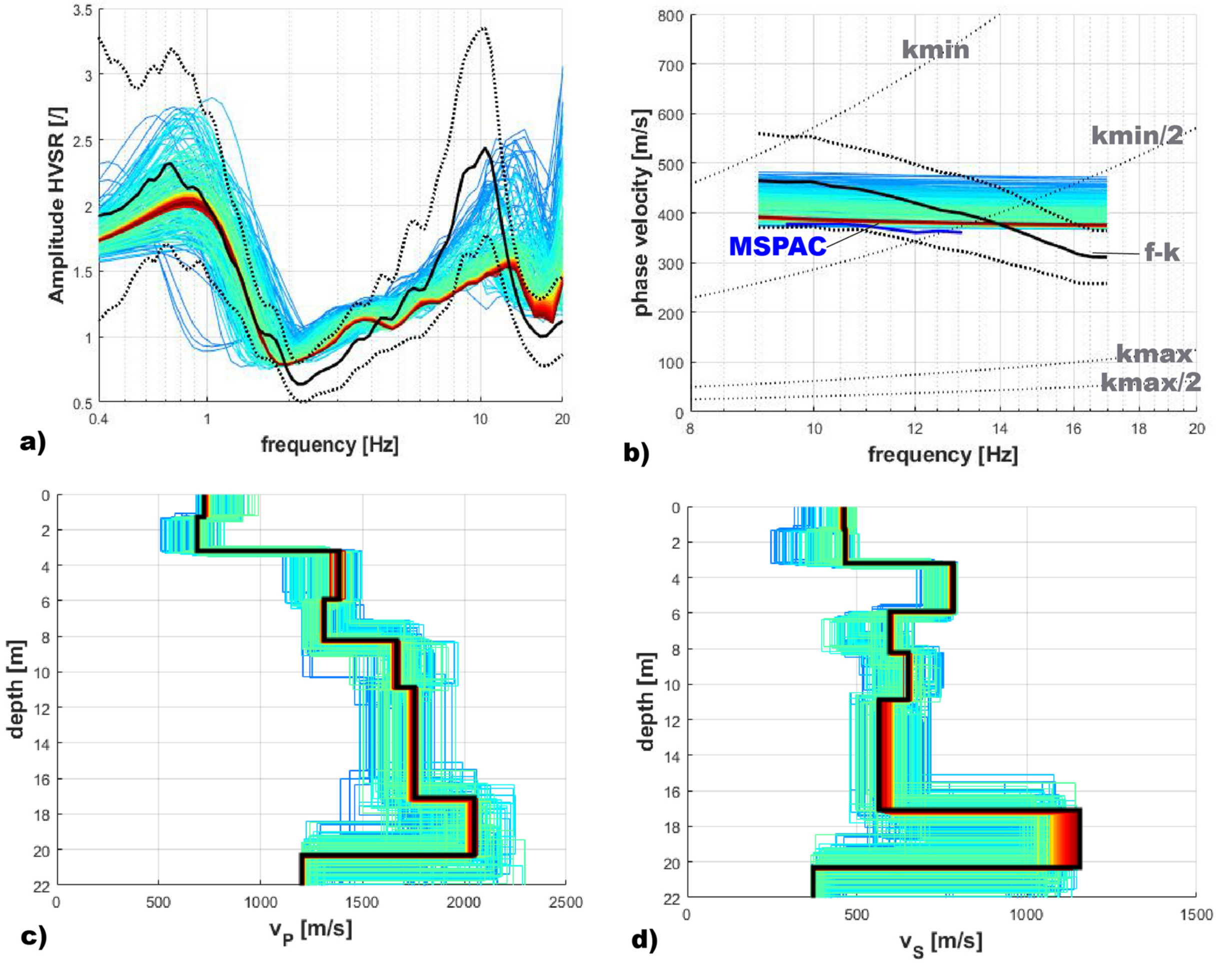

**Fig. 9** Results from 2D array measurement. The theoretical models of the fundamental mode Rayleigh-wave, in terms of ellipticity curves and dispersion, are shown in (**a**) and (**b**), respectively. The colour scale is proportional to the misfit resulting from the inversion, and the black curves are the measured dispersion and HVSR curves. The phase velocities in panel b are retrieved by the application of two methods (**f–k** and MSPAC) used for the processing of the 2D array recording. $V_P$ and $V_S$ models are shown in (**c**) and (**d**), respectively

**Table 1** Soil-gas data collected along two profiles (location in Fig. 3)

| Distance from borehole | $CO_2$ | $^{222}Rn$ |
|---|---|---|
| m | %. v/v | kBq/m$^3$ |
| *Profile 1* | | |
| 2 | 3.6 | 5.79 |
| 20 | 3.2 | 4.40 |
| 40 | 2.2 | 5.24 |
| 80 | 1.4 | 5.36 |
| 90 | 1.0 | 3.61 |
| 100 | 0.8 | 1.04 |
| 110 | 4.0 | 6.97 |
| 120 | 1.0 | 2.46 |
| 130 | 3.2 | 3.28 |
| 140 | 10.6 | 6.84 |
| 150 | 1.6 | 4.67 |
| 160 | 3.6 | 5.54 |
| 180 | 1.6 | 5.55 |
| 220 | 0.6 | 1.47 |
| 260 | 0.6 | 1.53 |
| *Profile 2* | | |
| 9 | 3.6 | 5.79 |
| 18 | 1.0 | 3.14 |
| 27 | 2.8 | 6.68 |
| 36 | 3.0 | 7.98 |

floods from the Tiber (middle-late Holocene, ~ 6 ka), which display a low resistivity (below 15 Ω × m); the travertine layer, at depths between 9 and 12 m, and with an intermediate resistivity (Zone 2, green to yellow in Figs. 4 and 10c) between 15 and 30 Ω × m; beneath the travertine unit, the resistivity decreases again below 15 Ω × m, and this zone matches the alluvial sediments (silt and silty sands) attributed to the lower portion of the buried terrace (Upper Pleistocene) and to the underlying Paleotiber unit (Middle Pleistocene) in the core stratigraphy. These measures were fundamental for attributing characteristic resistivities to the local deposits, which, in comparison with values from the literature for the same sediments are generally low, especially those of the travertine (Pola et al. 2014; Huerta et al. 2016; Török et al. 2019). This behaviour can be attributed to the quantity and quality of groundwater that almost reaches the field level and is particularly mineralised (the electrical conductivity of water is 3080 µS/cm; Giustini et al. 2018), generally reducing the resistivity (Loke and Barker 1996; Loke and Dahlin 2002; Oudeika et al. 2020).

At depths greater than 20 m, at a distance between 70 and 130 m from the origin of the profile, a zone with resistivity values higher than 30 Ω × m (Zone 3), showing a sharp lateral variation of resistivity, is observed. There are no borehole data that could aid in directly constraining the interpretation of this zone; however, considering the stratigraphic architecture of the Tiber valley, this zone could be related both to gravels and sands from the basal channel of the Paleotiber unit and/or to an even lower-occurring travertine body. The HVSR curves agree with both interpretations. In fact, the GF1 to GF7 sites (Fig. 10b) show an inversion of S-wave velocities in the soil profile (i.e., with the presence of layers with a lower velocity with respect to the upper ones) which is consistent with lithoid materials such as travertine and/or well-cemented gravels.

In the middle part of ERT-1, a wide zone of low resistivity values (< 15 Ω × m) may be ascribed to saturated deposits (probably silty and sandy alluvial sediments, based on the stratigraphic correlation; Giustini et al. 2020), characterised by a remarkable presence of mineralised waters. Corresponding to this part of the section, the soil-gas profile shows two peaks of $CO_2$ and $^{222}Rn$ concentrations (Fig. 10a). Overall, low resistivity values and soil-gas anomalies suggest the presence of a zone of intense water-fluid circulation, possibly associated with the presence of a structural or buried morphological discontinuity (perhaps represented by the sharp lateral variation between Zones 2 and 3 of the ERT) which allows the ascent of thermal waters and/or gas emissions. A $CO_2$-rich gas phase of deep origin (metamorphic and partly mantle/magma degassing) is associated with the Prima Porta borehole, and several gas vents, locally connected with crustal structural lineaments, have been documented along the Tiber valley (Vaselli et al. 1997; Minissale et al. 2002; Giustini et al. 2018). Generally, deep-gas leakage is facilitated by faults and fractures because they are deep, weakened zones consisting of highly fractured materials that increase permeability at the surface. The migration of $CO_2$ and $^{222}Rn$ by diffusion and/or advection along buried active faults can generate shallow anomalies with concentrations significantly higher than background levels. Radon, a radioactive inert gas with a half-life of 3.82 days, is particularly sensitive to buried discontinuities because of its ability to migrate along relatively long distances from host rocks, using $CO_2$ as carrier gas (King et al. 1996; Ciotoli et al. 2007, 2014, 2016).

A fractures system in this part of the section could be also supported by the wavefield polarisation analysis. At frequencies > 6 Hz, the GF5, GF6, GF7, and GF8 sites show a slight polarisation, with an azimuth of N0-20°; a slight polarisation is observed for sites GF1, GF3, and GF4 with an azimuth of N80-100° (Fig. 8). Moreover, a further preferential direction is enhanced from the rotational HVSR at

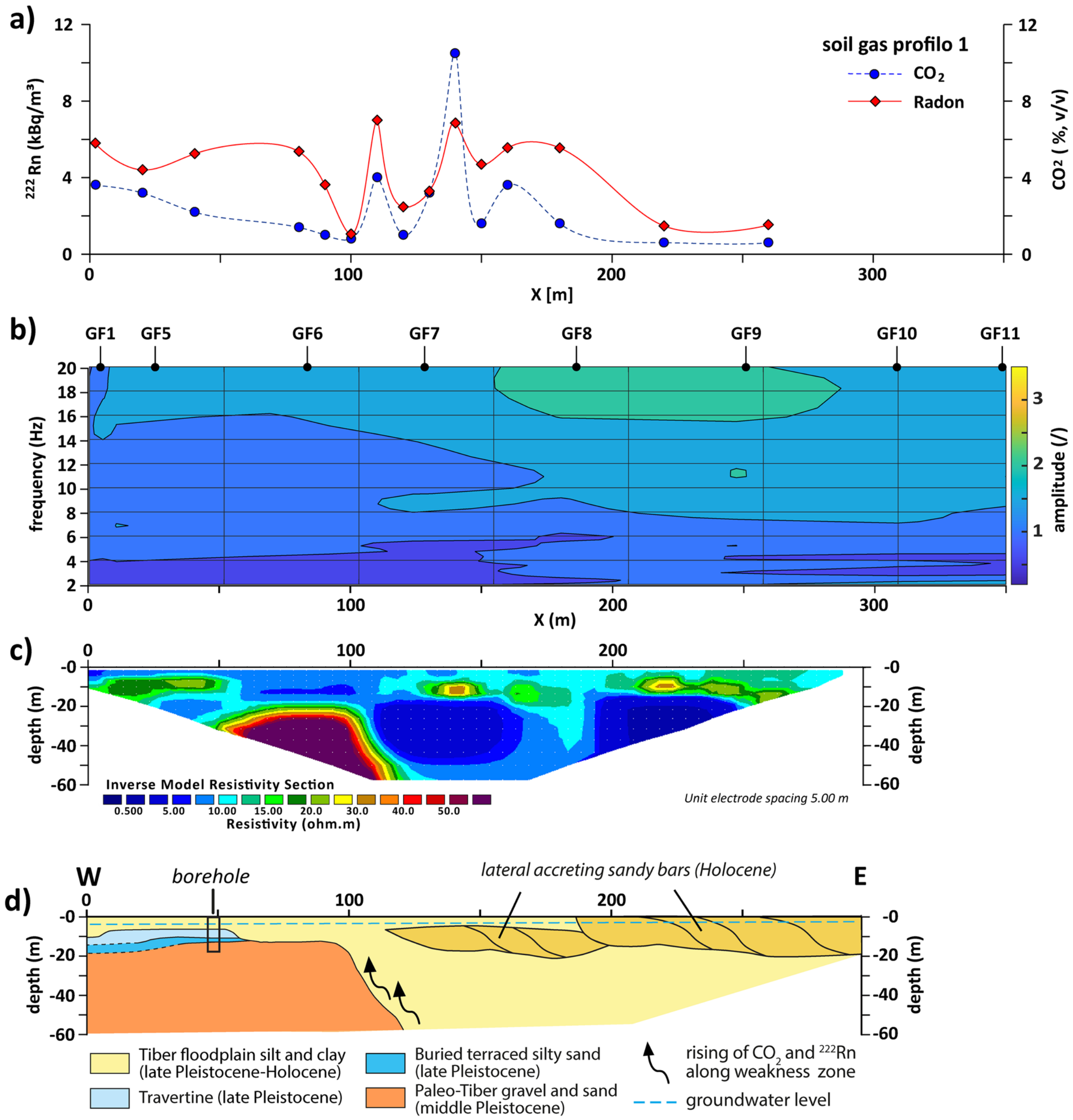

**Fig. 10** **a** Soil-gas ($CO_2$ and radon) profiles; **b** HVSR cross-section; **c** ERT-1; **d** geological interpretation of the ERT-1 profile

GF5, Gf6, GF7 and GF8: the measurements at GF5 and GF6 sites show amplification in the band about N160-180°, while the measurements at GF7 and GF8 sites show amplification in a wider azimuthal range (about N120-180°). To discuss the rationale behind this evidence, it should be underlined that buried fault zones may be very challenging to investigate due to the complex geological structures (i.e., S-wave velocity inversion with depth) in which the combination of several phenomena of wave propagation (reflection, resonance, Love wave trapping) modifies components with different weights and may render the interpretation difficult. Nevertheless, many authors have demonstrated that, in fault zones, horizontal polarisation is often strong and tends to be perpendicular to the fracture field or has a high-angle relative to the fault strike (Pischiutta 2010, Pischiutta et al. 2012, 2013, 2017; Napolitano et al. 2018 and reference therein; Panzera et al. 2016, 2017). The polarisation of the particle motion of seismic noise is also known to be modified by heterogeneities in a local structure such as cleavages or fractures (Ben-Zion 1998; Pischiutta et al. 2012). Famiani et al. (2015) also identified peaks that were broader and with lower amplitude and an important difference in terms of the signal polarisation across a seismogenic fault in central Italy (i.e., Pizzoli fault). Therefore, the observed polarisation in our data, further joined with the geochemical observations discussed above, and the local fracture trends (N90-110°)

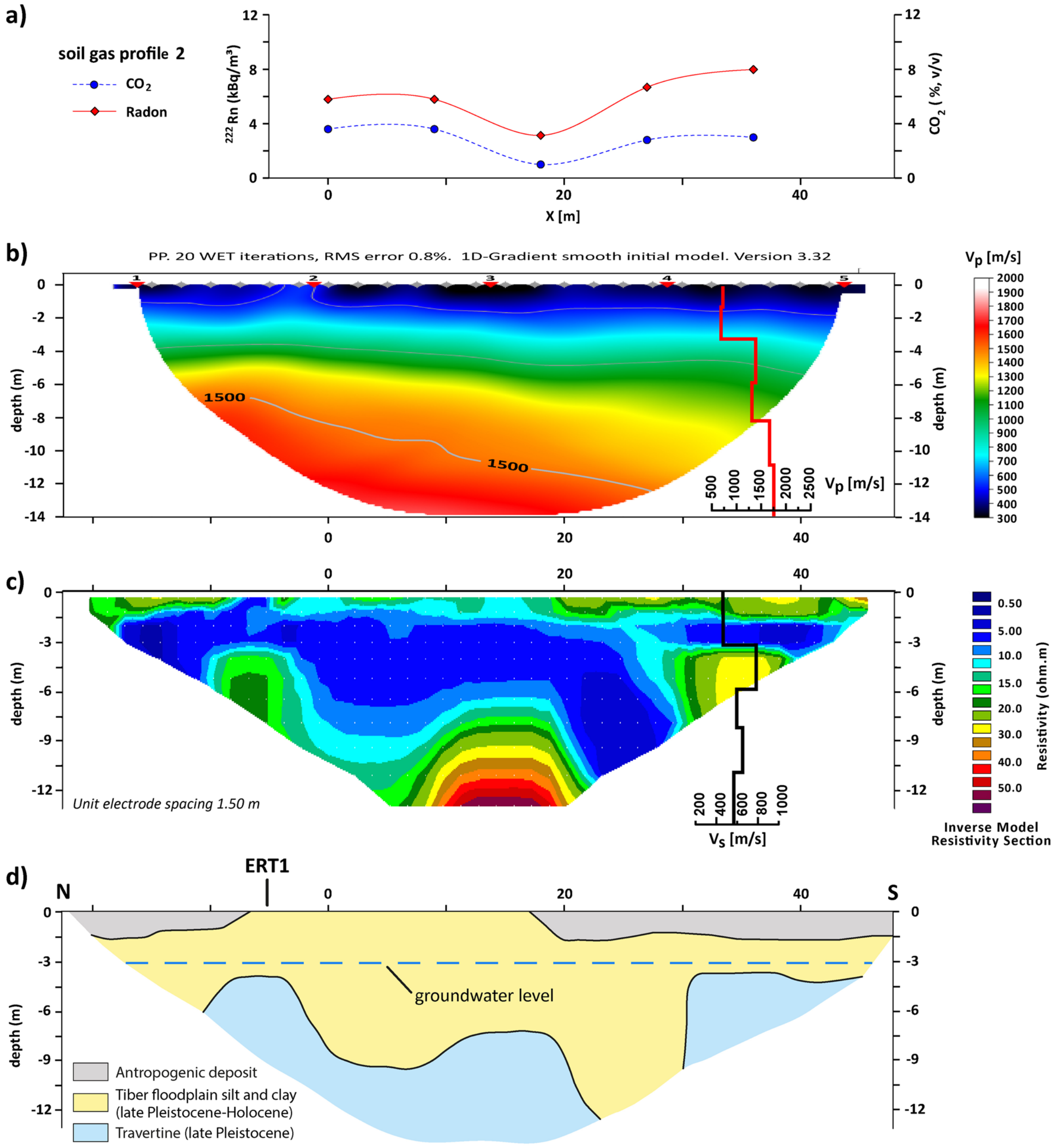

**Fig. 11** **a** Soil-gas ($CO_2$ and radon) profiles; **b** $V_P$ profile from the 2D array superimposed on SR section; **c** $V_S$ profile from the 2D array superimposed on ERT-2; **d** geological interpretation of the ERT-2 profile

traced in Fig. 1, let us hypothesize a role of the fracture systems (i.e., cracks) in the amplification at the study site.

In the eastern part of ERT-1, the resistivity Zone 2 overlies the high conductivity zone; it is located approximately at the same level as the travertine deposit intercepted by the borehole. According to the resistivity values, this zone might be interpreted on a first approximation as a large travertine body, extending between 150 m and the eastern end of the ERT, slightly dipping towards the present-day Tiber river's course. However, the HVSR curves and soil-gas concentrations do not bolster this interpretation. The HVSR curves, measured at the GF8, GF9 sites, show a very broad band peak at higher frequencies (Figs. 5 and 7). Otherwise, the HVSR amplitude values in Fig. 10b at about 50 m from the start of the W-E measurements alignment are lower than those measured in correspondence with the borehole; this configuration is coherent with a relatively surficial horizon of materials with poor mechanical properties such as relatively loose sands. This interpretation is confirmed by the low soil-gas concentrations measured with respect to the other parts of the profile (Fig. 10a), typical of a very ventilated soil. Therefore, this resistivity zone can be interpreted

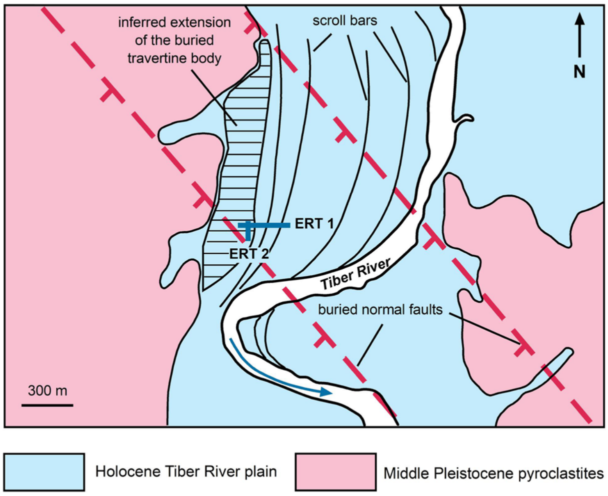

**Fig. 12** Sketch map showing the eastward-directed and convex-shaped scroll bars and the supposed extension of the buried travertine body. The buried inferred normal faults are from Funiciello et al. (1992)

as being due to the lateral stack of sandy channel-fill bodies, consisting of eastward-migrating bars and featuring the multilateral stacking pattern of channel bodies (Rajchl and Uličný 2005; Gibling 2006), which is a typical expression of the channel clustering in the TDS' late transgressive and highstand systems tracts (Milli et al. 2016). The laterally migrating bars in cross-sectional view corresponding to the scroll bars on a plane shown in Fig. 12. Relatively high resistivity sand-dominated channel-fill bodies, which are embedded into more conductive floodplain fines, have commonly been revealed by ERT investigations (Baines et al. 2002; Bersezio et al. 2007; Nimnate et al. 2017; Guinea et al. 2018).

The two ERT arrays have a point of intersection between electrodes n. 7 (of the ERT-2) and n. 40 (of the ERT-1), and ERT-2 also intercepts the travertine body, at a depth of about 4 m. In this tomography (Fig. 11c), travertine displays a concave-upward section wedging out toward the central part of the profile; here, the resistivity tends to increase up to 50 $\Omega \times$ m. A seismic refraction (SR) survey was performed above this high resistivity block; this measure allows one to constrain the S-wave profile obtained throughout the 2D array measurement (Fig. 11b) and to further confirm the interpretation of this block as a unique travertine body. In fact, S-wave velocity increases up to 800 m/s in correspondence with the high resistivity block, values that are compatible with compact and massive materials (Forte et al. 2019). In contrast, the Zones 2 of resistivity, which are about 1.5 m thick and located just below surface in the northern and southern parts of the profile, are not attributed to travertine, but to anthropogenic deposits—possibly a buried basement of an old edifice whose perimeter is still recognisable in old satellite images. The other zones of lower resistivity ($< 15$ $\Omega \times$ m) were interpreted as alluvial deposits covering the travertine.

Considering as a whole the high-strength structures of the two profiles, the upper surface of the travertine deposit appears to have a curved shape, which is gently dipping towards the east (i.e., towards the present-day Tiber river), and forms a concave-upward section wedging out toward the south; the maximum thickness could be 20 m. This curved shape is consistent with the morphology inferred from macroscopic and microfacies observations (Giustini et al. 2020), a pool in a terraced slope dam that is gently dipping towards the south and east. The real extension of the buried travertine body is unknown, but we speculate that it is roughly extended along an N-S direction, along the western border of the plain (Fig. 12), between the normal faults with roughly an NW–SE direction inferred from Funiciello et al. (1992). Ancient springs were probably connected to these structural features and related to the rising hydrothermal fluids precipitating travertine.

The combined application of these ERT, seismic refraction, ambient noise measurements, and soil-gas survey methodologies may be successfully used in similar geological contexts for identifying buried travertine bodies and other complex 2D/3D structures. The alluvial valleys are often located in tectonically active areas, similarly to the Tiber valley; travertine deposits can be quite common along their boundaries because they are associated with rising hydrothermal fluids, whose ascent is favoured by the presence of structural discontinuities. In these contexts, travertine deposits can potentially represent valuable archives of paleo-sources of $CO_2$ in places where gas emanations are no longer visible, evidencing active tectonics and low-enthalpy geothermal areas.

## Conclusions

The alluvial deposits of the Tiber river, at the Prima Porta site, were investigated using non-invasive geophysical and geochemical methods. The results were calibrated and interpreted using previously collected litho-stratigraphic data from a borehole drilled in the study area. The applied geophysical and geochemical techniques (ERT, seismic refraction, ambient noise measurements, and $CO_2$ and $^{222}$Rn concentrations in soil-gas surveys) complement each other and their combination allowed us to delineate the subsoil structure of this sector of the Tiber valley. In particular, the geometry of the buried travertine body of Prima Porta was defined; its upper surface appears to have a curved shape, gently dipping towards the east to the present-day Tiber river, and forming a concave-upward section wedging out toward the south. Due to its hydrothermal origin, this travertine unit is a poorly porous, hard and crystalline material, and consequently its specific electrical resistivity values were relatively high with respect to those measured in the embedding alluvial sediments (silt and silty sands). This shape is consistent with the morphology inferred from macroscopic and microfacies observations, i.e., a pool in a terraced slope dam (Giustini et al. 2020). Other stratigraphic and structural features of this sector of the Tiber valley were inferred, such as the presence of silty-sand channels, deposited by the Tiber river after the last glacial maximum. Finally, a weakness zone, permeable to the ascent of $CO_2$ and $^{222}$Rn, was inferred in correspondence with a low resistivity zone, a soil-gas anomaly, and slight polarisation effects recorded in the HVSR.

**Supplementary Information** The online version contains supplementary material available at https://doi.org/10.1007/s00531-022-02254-6.

**Acknowledgements** The authors are grateful to Gian Paolo Cavinato (IGAG-CNR) for his constructive comments and continue encouragement, and for providing software facilities for graphical elaborations. Prof. Giuseppe Della Monica and Francesco Basile (DST –Roma 3) are thanked for providing geophysical instruments for the ERT measurements and seismic refraction survey, and for the help during the geophysical survey, respectively. We also sincerely thank Azienda Agricola Orti del Canottiere, Giuseppe Capelli and Livio Manzetti for permitting access to the study area. This study was partly funded by DTA.AD003.316 "Sistemi terrazzati" Project, Resp. Marco Mancini. The authors sincerely thank Jozef Müller, Andreas Goepel and the topic editor Thomas Voigt for their constructive comments and suggestions.

## Declarations

**Conflict of interest** None of the material reported in the work has been published or is under consideration for publication elsewhere. Authors have no conflict of interest with any of the material presented.

## References

Asokhai MB, Egbai JC, Okolie EC (2008) Using shallow reflection seismology for mapping bedrocks. Nigerian J Sci Environ 7:66–72

Ayolabi EA, Adeoti L, Oshinlaja NA, Adeosun IO, Idowu OI (2009) Seismic refraction and resistivity studies of part of Igbogbo township, south-west Nigeria. J Sci Res Dev 11:42–61

Baines D, Smith DG, Froese DG, Bauman P, Nimeck G (2002) Electrical resistivity ground imaging (ERGI): a new tool for mapping the lithology and geometry of channel-belts and valley-fills. Sedimentology 49:441–449

Barberi F, Buonasorte G, Cioni R, Fiordelisi A, Foresi L, Iaccarino S, Laurenzi MA, Sbrana A, Vernia A, Villa IM (1994) Plio-Pleistocene geological evolution of the geothermal area of Tuscany and Latium. Memorie Descrittive Della Carta Geologica D'Italia 49:77–135

Beaubien SE, Jones DG, Gal F, Barkwith AKAP, Braibant G, Baubron J-C, Ciotoli G, Graziani S, Lister TR, Lombardi S, Michel K, Quattrocchi F, Strutt MH (2013) Monitoring of near-surface gas geochemistry at the Weyburn, Canada, CO2-EOR site, 2001–2011. Int J Greenhouse Gas Control 16:S236–S262. https://doi.org/10.1016/j.ijggc.2013.01.013

Ben-Zion Y (1998) Properties of seismic fault zone waves and their utility for imaging low-velocity structures. J Geophys Res Solid Earth 103(B6):12567–12585

Bersezio R, Giudici M, Mele M (2007) Combining sedimentological and geophysical data for high-resolution 3-D mapping of fluvial architectural elements in the Quaternary Po plain (Italy). Sed Geol 202:239–248

Bettig B, Bard PY, Scherbaum F, Riepl J, Cotton F, Cornou C, Hatzfeld D (2005) Analysis of dense array noise measurements using the modified spatial auto-correlation method (SPAC): application to the Grenoble area. Bollettino Di Geofisica Teorica e Applicata 42:281–304

Bridge JS (2003) Rivers and floodplains: forms, processes and sedimentary record. Blackwell, Oxford, p 491

Carlucci, G., 2017. *Ambient noise data Analysis for the reconstruction of the deep subsurface model in the roman area*. PhD thesis, University of Roma 3, Italy.

Castellaro S, Mulargia F (2009) The effect of velocity inversions on H/V. Pure Appl Geophys 166(4):567–592

Chiemeke CC, Aboh HO (2012) Delineation of aquiferous layers within the basement complex using joint inversion of seismic refraction tomography and high resolution 3D seismic reflection survey. Arch Appl Sci Res 4:400–405

Ciotoli G, Lombardi S, Annunziatellis A (2007) Geostatistical analysis of soil gas data in a high seismic intermontane basin: Fucino Plain, central Italy. J Geophys Res 112:B05407. https://doi.org/10.1029/2005JB004044

Ciotoli G, Bigi S, Tartarello C, Sacco P, Lombardi S, Ascione A et al (2014) Soil gas distribution in the main coseismic surface rupture zone of the 1980, Ms = 6.9, Irpinia earthquake (southern Italy). J Geophys Res Solid Earth 119:2440–2461. https://doi.org/10.1002/2013JB010508

Ciotoli G, Etiope G, Marra F, Florindo F, Giraudi C, Ruggiero L (2016) Tiber delta CO2-CH4 degassing: a possible hybrid, tectonically active Sediment-Hosted Geothermal System near Rome. Journal of Geophysical Research Solid Earth 121:48–69. https://doi.org/10.1002/2015JB012557

Cosentino, D., Cipollari, P., Marsili, P., Scrocca, D., 2010. Geology of the central Apennines: a regional review. In: Beltrando, M., Peccerillo, A., Mattei, M., Conticelli, S., Doglioni, C., (Eds.) *The Geology of Italy: tectonics and life along plate margins*. Journal of the Virtual Explorer, Electronic Edition, 36(12), doi: https://doi.org/10.3809/jvirtex.2010.00223.

De Filippis L, Anzalone E, Billi A, Faccenna C, Poncia PP, Sella P (2013) The origin and growth of a recently-active fissure ridge travertine over a seismic fault, Tivoli, Italy. Geomorphology 195:13–26

Di Bella L, Carboni MG, Bergamin L (2002) Pliocene-Pleistocene foraminiferal assemblages of the middle and lower Tiber Valley: stratigraphy and paleoecology. Geol Romana 36:129–145

Faccenna C (1994) Structural and hydrogeological features of Pleistocene shear zones in the area of Rome (Central Italy). Ann Geofis 37:121–133

Faccenna C, Funiciello R (1993) Tettonica pleistocenica tra il Monte Soratte e i Monti Cornicolani. Il Quaternario 6:103–118

Famiani, D., Amoroso, S., Boncio, P., Bordoni, P., Cantore, L., Cara, F., Di Giulio, G., Di Naccio, D., Hailemikael, S., Mercuri, A., Milana, G., Vassallo, M., 2015. Noise measurements along fault zones in central Appenines. In: 6th Int INQUA Meeting on Paleoseismology, Active Tectonics and Archaeoseismology, 19–24 April 2015, Pescina, Fucino Basin, Italy. INGV, 146–149.

Forte G, Chioccarelli E, De Falco M, Cito P, Santo A, Iervolino I (2019) Seismic soil classification of Italy based on surface geology and shear-wave velocity measurements. Soil Dyn Earthq Eng 122:79–93

Foti S, Hollender F, Garofalo F, Albarello D, Asten M, Bard P-Y, Comina C, Cornou C, Cox B, Di Giulio G, Forbriger T, Hayashi K, Lunedei E, Martin A, Mercerat D, Ohrnberger M, Poggi V, Renalier F, Sicilia D, Socco V (2018) Guidelines for the good practice of surface wave analysis: a product of the InterPACIFIC project". Bull Earthq Eng 16:2367–2420

Funiciello R, Parotto M (1978) Il substrato sedimentario nell'area dei Colli Albani: considerazioni geodinamiche e paleogeografiche sul margine tirrenico dell'Appennino centrale. Geol Romana 17:233–287

Funiciello R, Giuliani R, Marra F, Salvi S (1992) Superfici strutturali plio-quaternarie al margine sud-orientale del Distretto Vulcanico Sabatino. *Studi Geologici Camerti* spec. vol. 1991/2. CROP 11:301–304

Funiciello R, Giuliani R, Marra F, Salvi S (1994) The influence of volcanism and tectonics on Plio-Quaternary regional landforms in the Southeastern Sabatinian area (Central Italy). Memorie Descrittive Della Carta Geologica D'italia 49:323–332

Funiciello, R., Giordano, G., 2008. *Note illustrative della Carta Geologica d'Italia alla scala 1:50.000, Foglio 347 ROMA*. APAT–Servizio Geologico d'Italia, Roma

Funiciello R, Giordano G (2010) *The Colli Albani Volcano*. International Association of Volcanology and Chemistry of the Earth's Interior Special Publication 3, 400 pp.

Gabr A, Murad A, Baker H, Bloushi K, Arman H, Mahmoud S. (2012) The use of seismic refraction and electrical techniques to investigate groundwater aquifer, Wadi Al-ain, United Arab Emirates (UAE). In: Proceedings of the International Conference on Water Resources and Wetlands Sept. 14–16, Tulcea-Romania, 94–99.

García-Jerez A, Piña-Flores J, Sánchez-Sesma FJ, Luzón F, Perton M (2016) A computer code for forward calculation and inversion of the H/V spectral ratio under the diffuse field assumption. Comput Geosci 97:67–78. https://doi.org/10.1016/j.cageo.2016.06.016

García-Jerez A, Luzón F, Sánchez-Sesma FJ, Lunedei E, Albarello D, Santoyo MA, Almendros J (2013) Diffuse elastic wavefield within a simple crustal model. Some consequences for low and high frequencies. J Geophys Res 118(10), 5577–5595. https://doi.org/10.1002/2013JB010107

Gibling MR (2006) Width and thickness of fluvial channel bodies and valley fills in the geological record: a literature compilation and classification. J Sediment Res 76:731–770

Giustini F, Brilli M, Mancini M (2018) Geochemical study of travertines along middle-lower Tiber valley (central Italy): genesis, palaeo-environmental and tectonic implications. Int J Earth Sci 107:1321–1342

Giustini F, Brilli M, Di Salvo C, Mancini M, Voltaggio M (2020) Multidisciplinary characterization of the buried travertine body of Prima Porta (Central Italy). Quatern Int 568:65–78

Guinea A, Hollins S, Meredith K, Hankin S, Cendón DI (2018) Characterization of the subsurface architecture and identification of potential groundwater paths in a clay-rich floodplain using multi-electrode resistivity imaging. Hydrol Sci J 63:909–925

Hinkle ME (1994) Environmental conditions affecting concentrations of He, $CO_2$, $O_2$ and $N_2$ in soil gases. Appl Geochem 9(1):53–63

Huerta P, Armenteros I, Tomé OM, Gonzálvez PR, Silva PG, González-Aguilera D, Carrasco-García P (2016) 3-D modelling of a fossil tufa outcrop. The example of La Peña del Manto (Soria, Spain). Sed Geol 333:130–146

Igboekwe MU, Ohaegbuchu HE (2011) Investigation into the weathering layer using up-hole method of seismic refraction. J Geol Min Res 3:73–86

Kilner M, West LJ, Murray T (2005) Characterisation of glacial sediments using geophysical methods for groundwater source protection. J Appl Geophys 57:293–305. https://doi.org/10.1016/j.jappgeo.2005.02.002

King CY, King BS, Evans WC, Zang W (1996) Spatial radon anomalies on active faults in California. Appl Geochem 11:497–510

Klusman RW (1993) Soil gas and related methods for natural resource exploration. Wiley, England, p 483

Konno K, Ohmachi T (1998) Ground-motion characteristics estimated from spectral ratio between horizontal and vertical components of microtremors. Bull Seismol Soc Am 88:228–241

Lacoss R, Kelly TEJ, Toksöz MN (1969) Estimation of seismic noise structure using arrays. Geophysics 34(1):21–38

Loke MH, Barker RD (1996) Practical technique for 3D resistivity surveys and data inversion. Geophys Prospect 44:499–523

Loke MH, Dahlin T (2002) A comparison of Gauss-Newton and quasi-Newton methods in resistivity imaging inversion. J Appl Geophys 49:149–162

Lunedei E, Malischewsky P (2015) A review and some new issues on the theory of the H/V technique for ambient vibrations. In: Ansal A (Ed.) Perspectives on European Earthquake Engineering and Seismology*,* Springer, Berlin, 371–394. https://doi.org/10.1007/978-3-319-16964-4_15

Malinverno A, Ryan WBF (1986) Extension of the Tyrrhenian Sea and shortening in the Apennines as result of arc migration driven by sinking lithosphere. Tectonics 5:227–245

Mancini M, D'Anastasio E, Barbieri M, De Martini PM (2007) Geomorphological, paleontological and $^{87}$Sr/$^{86}$Sr isotope analyses of early Pleistocene paleoshorelines to define the uplift of Central Apennines (Italy). Quatern Res 67(3):487–501

Mancini M, Cavinato GP, (2005) The Middle Valley of the Tiber River, central Italy: Plio-Pleistocene fluvial and coastal sedimentation, extensional tectonics and volcanism. In: Blum, M.D., Marriott, S.B., Leclair, S.F. (Eds.), Fluvial sedimentology. IAS Special Publication, vol. 35, Blackwell, Oxford, pp. 373–396.

Marcucci S, Milana G, Hailemikael S, Carlucci G, Cara F, Di Giulio G, Vassallo M (2019) The deep bedrock in Rome, Italy: a new constraint based on passive seismic data analysis. Pure Appl Geophys 176(6):2395–2410

Martinson DG, Pisias NG, Hayes JD, Imbrie J, Moore TC, Shackleton NJ (1987) Age dating and the orbital theory of the ice ages development of a highresolution 0 to 300,000 year chronostratigraphy. Quatern Res 27:1–29

Miall AD (2014) Fluvial Depositional Systems. Springer, Cham, p 316

Milli S, Mancini M, Moscatelli M, Stigliano F, Marini M, Cavinato GP (2016) From river to shelf, anatomy of a high-frequency depositional sequence: the late Pleistocene to Holocene Tiber depositional sequence. Sedimentology 63:1886–1928

Minissale A, Kerrick DM, Magro G, Murrell MT, Paladini M, Rihs S, Sturchio NC, Tassi F, Vaselli O (2002) Geochemistry of Quaternary travertines in the region north of Rome (Italy): structural, hydrologic and paleoclimatic implications. Earth Planet Sci Lett 203:709–728

Nakamura Y (1989) A method for dynamic characteristics estimation of subsurface using microtremor on the ground surface. Q Report Railway Tech Res Inst 30:25–33

Napolitano F, Gervasi A, La Rocca M, Guerra I, Scarpa R (2018) Site Effects in the Pollino Region from the HVSR and Polarization of Seismic Noise and Earthquakes Site Effects in the Pollino Region from the HVSR and Polarization of Seismic Noise and Earthquakes. Bull Seismol Soc Am 108(1):309–321

Nimnate P, Thitimakorn T, Choowong M, Hisada K (2017) Imaging and locating paleo-channels using geophysical data from meandering system of the Mun River, Khorat Plateau, Northeastern Thailand. Open Geosciences 9:675–688

Okiongbo KS, Akpofure E, Odubo E (2011) Determination of aquifer protective capacity and corrosivity of near surface materials in Yenagoa city, Nigeria. Res J Appl Sci Eng Technol 3:785–791

Oudeika MS, İlkimen EM, Taşdelen S, Aydin A (2020) Distinguishing Groundwater Flow Paths in Fractured Rock Aquifers Formed Under Tectonic Stress Using Geophysical Techniques: Cankurtaran Basin, Denizli, Turkey. Int J Environ Res 14:567–581

Panzera F, Lombardo G, Monaco C (2016) New evidence of wavefield polarization on fault zone in the lower NE slope of Mt. Etna Italian J Geosci 135(2):250–260

Panzera F, Lombardo G, Longo E, Langer H, Branca S, Azzaro R, Cicala V, Trimarchi F (2017) Exploratory seismic site response surveys in a complex geologic area: a case study from Mt. Etna volcano (southern Italy). Nat Hazards 86(2):385–399

Patacca E, Sartori R, Scandone P (1990) Tyrrhenian basin and Apenninic arcs: Kinematics relations since Late Tortonian times. Memorie Della Società Geologica Italiana 45:425–451

Piña-Flores J, Perton M, García-Jerez A, Carmona E, Luzón F, Molina-Villegas JC, Sánchez-Sesma FJ (2017) The inversion of spectral ratio H/V in a layered system using the diffuse field assumption (DFA). Geophys J Int 208:577–588

Pischiutta M (2010) The polarization of horizontal ground motion: an analysis of possible causes. Ph.D. thesis, Università di Bologna 'Alma Mater Studiorum', Italy

Pischiutta M, Salvini F, Fletcher J, Rovelli A, Ben-Zion Y (2012) Horizontal polarization of ground motion in the Hayward fault zone at Fremont, California: dominant fault-high-angle polarization and fault-induced cracks. Geophys J Int 188(3):1255–1272

Pischiutta M, Anselmi M, Cianfarra P, Rovelli A, Salvini F (2013) Directional site effects in a non-volcanic gas emission area (Mefite d'Ansanto, southern Italy): Evidence of a local transfer fault transversal to large NW–SE extensional faults? Phys Chem Earth Parts a/b/c 63:116–123

Pischiutta M, Fondriest M, Demurtas M, Magnoni F, Di Toro G, Rovelli A (2017) Structural control on the directional amplification of seismic noise (Campo Imperatore, central Italy). Earth Planet Sci Lett 471:10–18

Pola M, Gandin A, Tuccimei P, Soligo M, Deiana R, Fabbri P, Zampieri D (2014) A multidisciplinary approach to understanding carbonate deposition under tectonically controlled hydrothermal circulation: a case study from a recent travertine mound in the Euganean Hydrothermal System, northern Italy. Sedimentology 61:172–199

Qarqori K, Rouai M, Moreau F, Saracco G, Dauteuil O, Hermitte D, Boualoul M, Carlier Le, de Veslud C (2012) Geoelectrical Tomography Investigating and Modeling of Fractures Network around Bittit Spring (Middle Atlas, Morocco). International Journal of Geophysics 2012:489634. https://doi.org/10.1155/2012/489634

Rajchl M, Uličný D (2005) Depositional record of an avulsive fluvial system controlled by peat compaction (Neogene, Most Basin, Czech Republic). Sedimentology 52:601–625

De Rita, D., Funiciello, R., Corda, L., Sposato, A., Rossi, U., 1993. Volcanic Units. In: Di Filippo, M. (Ed.) *Sabatini Volcanic Complex*. Quaderni della Ricerca Scientifica, C.N.R., Roma, 114, 33–79.

Russell CE, Mountney NP, Hodgson DM, Colombera L (2018) A novel approach for prediction of lithological heterogeneity in fluvial point-bar deposits from analysis of meander morphology and scroll-bar pattern. In: Ghinassi, M., Colombera, L., Mountney, N.P., Reesnik, A.J.H. (Eds.) *Fluvial Meanders and Their Sedimentary Products in the Rock Record*. Int. Assoc. Sedimentol. Spec. Publ., 48, 385–418.

Sánchez-Sesma FJ (2017) Modeling and inversion of the microtremor H/V spectral ratio: physical basis behind the diffuse field approach. Earth Planets Space. https://doi.org/10.1186/s40623-017-0667-6,2017

Sánchez-Sesma FJ, Rodríguez M, Iturrarán-Viveros U, Luzón F, Campillo M, Margerin L, García-Jerez A, Suarez M, Santoyo MA, Rodríguez-Castellanos A (2011) A theory for microtremor H/V spectral ratio: application for a layered medium. Geophys J Int 186:221–225. https://doi.org/10.1111/j.1365-246X.2011.05064.x

Schumm SA (1993) River response to base level change: implications for sequence stratigraphy. J Geol 101:279–294

Sottili G, Palladino DM, Zanon V (2004) Plinian activity during the early eruptive history of the Sabatini Volcani District, Central Italy. J Volcanol Geoth Res 135:361–379

Tentori D, Marsaglia KM, Milli S (2016) Sand compositional changes as a support for sequence-stratigraphic interpretation: the Middle Upper Pleistocene to Holocene deposits of the Roman Basins (Rome, Italy). J Sediment Res 86:1208–1227

Török Á, Claes H, Brogi A, Liotta D, Tóth Á, Mindszenty A, Kudó I, Kele S, Huntington KW, Shen C-C, Swennen R (2019) A multi–methodological approach to reconstruct the configuration of a travertine fissure ridge system: The case of the Cukor quarry (Süttő, Gerecse Hills, Hungary). Geomorphology 345:106836

Varughese, A., Kumar, P., Kumar, N., 2011. Seismic refraction survey a reliable tool for subsurface characterisation for hydropower projects. *Proceedings of Indian Geotechnical Conference*, Dec. 15–17, Kochi, 137–139.

Vaselli O, Tassi F, Minissale A, Capaccioni B, Magro G, Evans WC (1997) Geochemistry of natural gas manifestations from the Upper Tiber Valley (Central Italy). Mineral Petrogr Acta 40:201–212

Ventriglia U (2002) Geologia del territorio del Comune di Roma. Provincia di Roma, Rome, p 810

Wathelet M, Chatelain JL, Cornou C, Giulio GD, Guillier B, Ohrnberger M, Savvaidis A (2020) Geopsy: a user-friendly open-source tool set for ambient vibration processing. Seismol Res Lett 91(3):1878–1889